Growth Anisotropy and Morphology Evolution of Line Defects in Monolayer MoS₂: Atomic-Level Observation, Large-Scale Statistics, and Mechanism Understanding

Shouheng Li, Jinguo Lin, Yun Chen, Zheng Luo, Haifeng Cheng, Feng Liu,* Jin Zhang, and Shanshan Wang*

Understanding the growth behavior and morphology evolution of defects in 2D transition metal dichalcogenides is significant for the performance tuning of nanoelectronic devices. Here, the low-voltage aberration-corrected transmission electron microscopy with an in situ heating holder and a fast frame rate camera to investigate the sulfur vacancy lines in monolayer MoS₂ is applied. Vacancy concentration-dependent growth anisotropy is discovered, displaying first lengthening and then broadening of line defects as the vacancy densifies. With the temperature increase from 20 °C to 800 °C, the defect morphology evolves from a dense triangular network to an ultralong linear structure due to the temperature-sensitive vacancy migration process. Atomistic dynamics of line defect reconstruction on the millisecond time scale are also captured. Density functional theory calculations, Monte Carlo simulation, and configurational force analysis are implemented to understand the growth and reconstruction mechanisms at relevant time and length scales. Throughout the work, high-resolution imaging is closely combined with quantitative analysis of images involving thousands of atoms so that the atomic-level structure and the large-area statistical rules are obtained simultaneously. The work provides new ideas for balancing the accuracy and universality of discoveries in the TEM study and will be helpful to the controlled sculpture of nanomaterials.

1. Introduction

Understanding the growth behavior and morphology evolution of materials is of great significance, which is especially true for 2D materials composed of surface atoms. On the micrometer scale, tremendous progress has been made. Various compact shapes (e.g., hexagons, rectangles, triangles, etc.) and dendritic domains have been thermodynamically or kinetically grown via tailoring the precursor concentration,[1–6] growth temperature,[7,8] and substrate symmetry (top panel of **Figure 1**),[9,10] which tunes the percentage and structure of edge atoms and inspires special electrocatalytic,[11–13] optical,[14] and magnetic performances.[15] On the atomic scale, the defect is an important object to investigate. For 2D transition metal dichalcogenides (TMDs, e.g., MoS₂, WS₂), researchers have studied the growth and morphology of diverse defects, such as cracks,[16–18] grain boundaries,[19–23] and dopant clusters,[24–27] which help unveil the failure mechanisms and adjust the

S. Li, Y. Chen, Z. Luo, H. Cheng, S. Wang
Science and Technology on Advanced Ceramic Fibers
and Composites Laboratory
College of Aerospace Science and Engineering
National University of Defense Technology
Changsha 410073, P. R. China
E-mail: wangshanshan08@nudt.edu.cn
S. Li, J. Zhang
Center for Nanochemistry
Beijing Science and Engineering Center for Nanocarbons
Beijing National Laboratory for Molecular Sciences
College of Chemistry and Molecular Engineering
Peking University
Beijing 100871, P. R. China

J. Lin, F. Liu
State Key Laboratory of Nonlinear Mechanics
Institute of Mechanics
Chinese Academy of Sciences
Beijing 100190, P. R. China
E-mail: liufeng@imech.ac.cn
J. Lin, F. Liu
School of Engineering Sciences
University of Chinese Academy of Sciences
Beijing 100049, P.R. China
J. Zhang, S. Wang
School of Advanced Materials
Peking University Shenzhen Graduate School
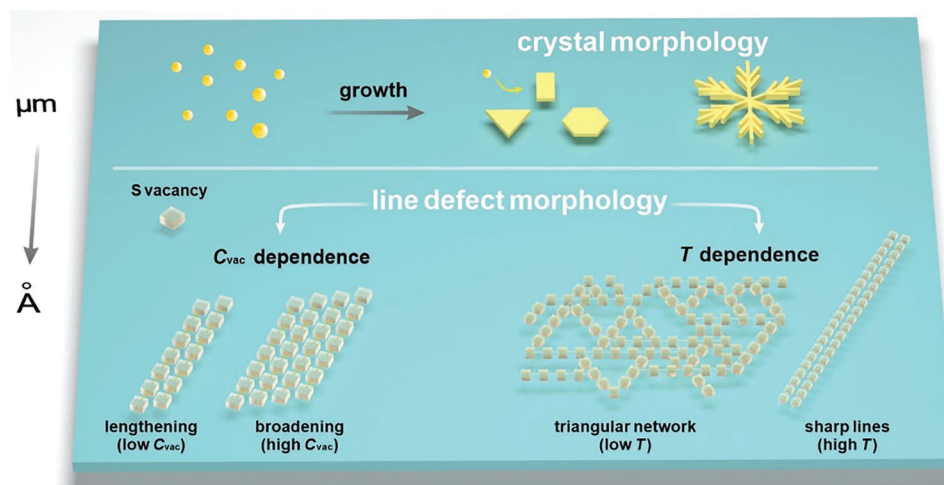Shenzhen 518055, P. R. China

Figure 1. Diagram showing the research idea of this work, which transfers the growth and morphology investigation paradigm of 2D crystals at the micrometer scale to the defect study at the atomic scale. C_{vac} represents the vacancy concentration.

electronic properties of 2D material-based flexible and nanoelectronic devices.[28,29]

As a representative line defect in 2D TMDs, the linearly arranged chalcogen vacancies[30–34] with locally changed stoichiometric ratio and chemical bonding have been widely concerned due to the special features such as smaller bandgaps,[31] high catalytic activity,[35,36] and unidirectional spin–orbit interaction.[37] Komsa et al. first demonstrated the staggered configuration of sulfur (S) vacancy lines by combining transmission electron microscopy (TEM) and density functional theory (DFT) calculations.[38] 4D scanning transmission electron microscopy (STEM) was then performed to directly map the 1D electron-rich channels at S vacancy lines in monolayer MoS_2 and WS_2.[39] Patra et al. combined genetic algorithm with molecular dynamics to investigate the evolution of line defects at relatively low vacancy concentrations (1.5–7.5%) and their role in inducing the 2H-1T phase transition in monolayer MoS_2.[40] In addition, the density and orientation of line defects can be affected by electron irradiation dose and external strain field,[38,41] while a high temperature can induce the ultralong linear defect configuration and the formation of novel 2D Mo_2S_3.[42,43] The as-grown line defects were also discovered to be dynamically unstable under the electron beam in monolayer $MoTe_2$, displaying migration, rotation, and local phase transition behaviors.[44,45]

However, there still remain limitations in the study of line defects in 2D TMDs. First, most of the previous work displays the atomic-scale structures of individual line defects in a small area through high-magnification (S)TEM images. How to, at the same time, quantitatively extract the structural information of defects in a large area is a question. Second, the growth and morphology of line defects are affected by various factors (e.g., temperature, vacancy concentration), but the detailed relationship and mechanisms between them have not been thoroughly understood. Third, the atomistic dynamics of line defects at high temporal resolution lack sufficient experimental and theoretical research. These deficiencies limit our insights into the growth and morphological evolution of line defects in 2D TMDs from

different temporal and spatial scales, from individual behavior to collective behavior, and from qualitative to quantitative.

Here, we combine high-resolution imaging with quantitative analysis of large-area AC-TEM images to study the S vacancy line growth behavior and morphology transition in monolayer MoS_2 under electron beam irradiation (bottom panel of Figure 1). The atomic-scale information and statistically significant results can be acquired simultaneously. The automatic identification of the atomic coordination states together with the transfer of the mathematical concept of "alloying degree" makes us quantitatively unveil the vacancy concentration-dependent growth anisotropy of the S vacancy lines. These line defects lengthen preferentially at low vacancy concentrations, and broadening is initiated as the vacancy densifies, whose mechanism has been thermodynamically verified by the DFT calculations. At a high vacancy density, a small area of monolayer MoS with decreased lattice symmetry is formed and theoretically predicted to exhibit anisotropy in mechanical, electrical, and thermal properties. Using an in-situ heating holder in the low-voltage AC-TEM, the morphology evolution of the S vacancy lines as a function of the growth temperature has also been systematically investigated and the mechanism is attributed to the vacancy diffusion process with the aid of Monte Carlo simulations. Finally, a fast frame rate camera is applied to track the atomistic dynamics of line defect reconstruction on the millisecond time scale. Configurational force analysis together with DFT calculations is performed to understand the energy optimization and the intermediate steps during the defect reconstruction.

2. Results and Discussion

We first qualitatively and quantitatively investigated the morphology evolution of S vacancy aggregates in monolayer MoS_2 over a relatively large range (≈1600 atoms per image) with increasing vacancy concentration at 20 °C (**Figure 2**). The monolayer MoS_2 was prepared by atmospheric pressure hydrogen-free chemical vapor deposition (see Experimental Section). The increase of S vacancy concentration was achieved by continuous electron beam
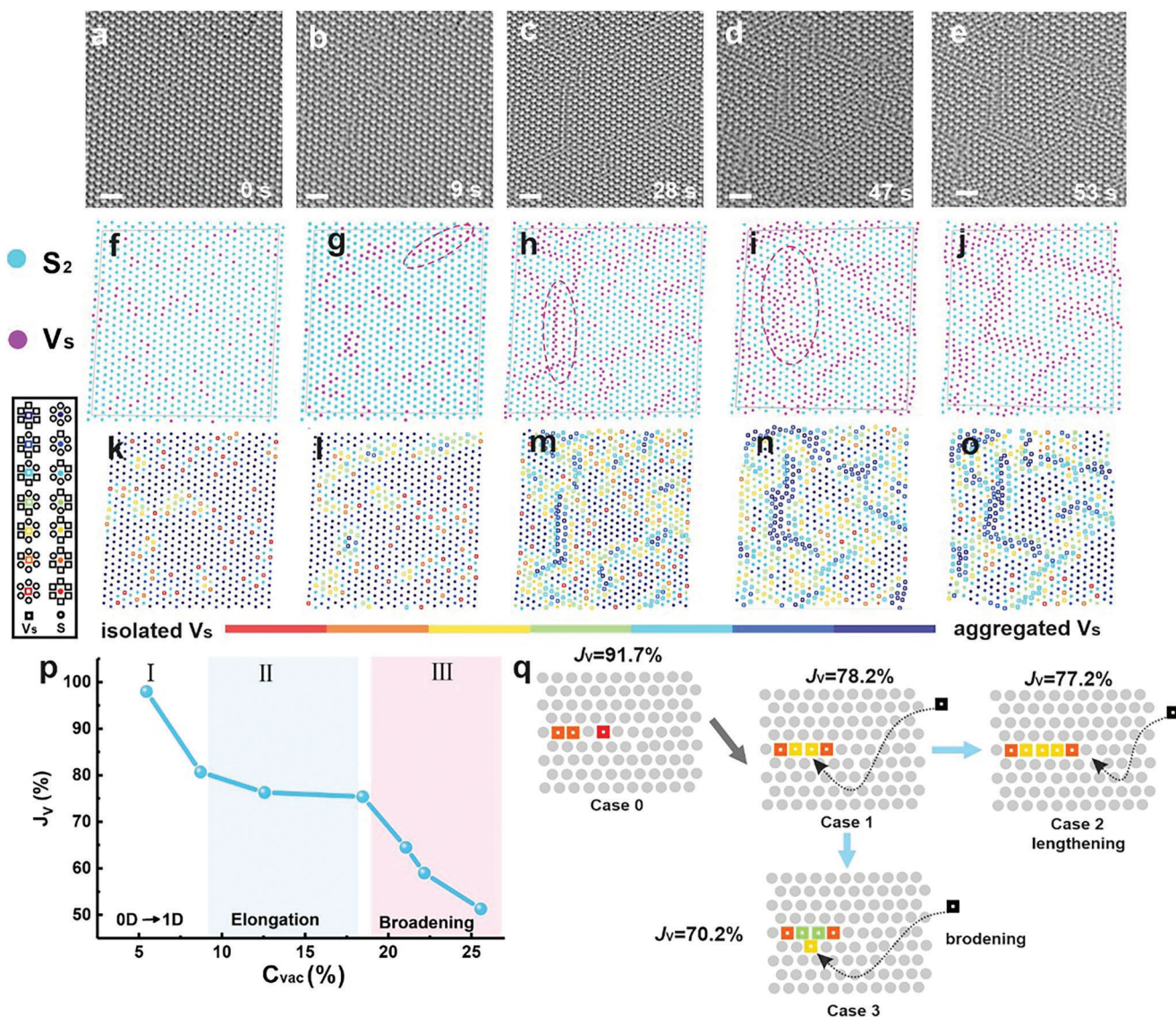
Figure 2. Quantitative analysis of morphological evolution of S vacancy aggregates as a function of vacancy concentration. a–e) Time series of AC-TEM images showing the S vacancy aggregation evolution in monolayer MoS_2 under continuous electron beam irradiation. Scale bars: 1 nm. f–j) Identification of S vacancy sites among all sulfur atomic columns. The double S sites (S_2) are marked by cyan spots, while the S vacancy sites (V_s) are highlighted by pink spots. k–o) Automatic identification of the coordination number of the nearest neighboring S_2 sites around each S vacancy in the projective view. Squares represent S vacancies, while spots represent disulfide atomic sites. Squares in red, orange, yellow, green, cyan, blue, and ultramarine represent S vacancies having six, five, four, three, two, one, and zero S_2 sites coordinated as the nearest neighbors, respectively. Spots in red, orange, yellow, green, cyan, blue, and ultramarine represent the disulfide sites having six, five, four, three, two, one, and zero S vacancies coordinated as the nearest neighbors, respectively. A color bar is situated at the bottom of panels k–o. The closer the color of the square representing the S vacancy is to the left of the color bar, the more discrete the vacancy distribution. In contrast, the closer the color of the square is to the right of the color bar, the more aggregated the vacancy distribution. p) Plot showing the alloying degree of S vacancies (J_V) as a function of vacancy concentration (C_{vac}). q) Schematic diagram illustrating the relation between the alloying degree J_V and the topology evolution of the vacancy aggregates.

irradiation of the suspended sample under the conditions of an accelerating voltage of 80 kV and electron dose of $\approx 10^5$ e$^-$ nm^{-2} s^{-1}. It is worth noting that, limited by the maximum energy that the electron beam can transfer to the atom at this accelerating voltage (≈ 6.5 eV), only S atoms rather than Mo atoms can be ejected and form vacancies.[31,33,46,47] Moreover, single S vacancies in which only one S atom is lost in non-metallic sites are dominant.[31,38] Figure 2a–e and Figure S1 (Supporting Information) are time series of AC-TEM images showing the structural

evolution of the same region of monolayer MoS_2 as the irradiation time prolongs. To highlight the change in the number of S vacancies and the morphology of aggregation, we applied software to perform contrast analysis on each atomic column and identified the position of S vacancies in every image containing ≈ 800 chalcogen atomic columns. It was found that with the extension of irradiation time, the quantity of S vacancies rises (Figure S2, Supporting Information). Their morphology evolves from isolated spots (Figure 2f) to short vacancy lines along zigzag

directions (red ellipse in Figure 2g), and then to long vacancy lines with 2–3 atomic columns wide (red ellipse in Figure 2h). Finally, when the S vacancies account for about 20%−25% of the total disulfide sites, the width of the line defect increases significantly with more than 4 side-by-side S vacancy lines frequently observed (red ellipse in Figure 2i,j).

Quantitative analysis of large-area AC-TEM images can achieve atomic-scale information and statistically significant conclusions simultaneously. Therefore, we transfer the concept of "alloying degree" in the alloy research to quantify the aggregation states of S vacancies, especially the morphology evolution after the formation of line defects in large-area AC-TEM images.[48] Mathematically, the alloying degree of S vacancies (J_v) can be expressed as

$$J_V = P(\text{observed}) / P(\text{random}) \times 100\% \tag{1}$$

$$P(\text{observed}) = \frac{\sum_{i=0}^{6} \left(i \times N_{V-iS} \right)}{6 \times N_V} \tag{2}$$

$$P(\text{random}) = \frac{N_S}{N_S + N_V} \tag{3}$$

in which P(observed) represents the ratio of the averaged coordination number of the disulfide atomic sites around a S vacancy to the total coordination number (six) of a S vacancy. P(random) represents the atomic ratio of S vacancy sites to all the non-metallic sites in monolayer MoS_2. N_V and N_S represent the total number of the S vacancy sites and the disulfide atomic sites in the examined area. N_{V-iS} indicates the number of the S vacancies that have i disulfide atomic sites coordinated around. The value of i can be from 0 to 6. Note that, we ignored Mo sites in this study and did not discriminate the S atoms at the top and bottom atomic planes in monolayer MoS_2. Such strategies to simplify the discussion have been applied in previous papers related to 2D alloys.[49–51]

The variation of J_V reflects the atomic-scale distribution of S vacancies in monolayer MoS_2, leading to different modes of agglomeration or segregation. When $J_V < 100\%$, it means that S vacancies prefer to aggregate with S vacancies rather than disulfide atomic sites and generate a homophilic structure. If $J_V > 100\%$, it means that S vacancies are prone to gather disulfide sites around and form a heterophilic configuration. If $J_V = 100\%$, no preference is seen for the arrangement of S vacancies and disulfide sites, leading to a randomly mixed atomic structure. By writing a program that can automatically analyze information including the type of the atomic sites and the distance of neighboring atoms, the coordination situation of each non-metallic site corresponding to AC-TEM images in panels a-e can be swiftly extracted in batches (Figure 2k–o and Figure S3, Supporting Information). Combining the coordination information in Figure 2k–o with Equations (1) to (3), we drew a plot showing the change of J_V as a function of the S vacancy concentration (C_{vac}), as shown in Figure 2p. The plot exhibits two characteristics: i) the J_V value is always smaller than 100%, indicating that S vacancies tend to agglomerate with themselves; ii) the decline rate of J_V (the slope of the curve) experiences three stages, namely the rapid decline period (stage I), the plateau period (stage II), and the secondary rapid decline period (stage III). These results quantitatively and statistically support that as the S vacancy concentration increases, the distribution of vacancies changes from isolated clusters to aggregated lines (stage I). More importantly, the growth of S vacancy lines exhibits prominent vacancy concentration-dependent growth anisotropy, which means they prefer to extend at a relatively low vacancy concentration (stage II) and then start to widen as the vacancy concentration goes higher (stage III).

To better understand the relationship between the slope of the J_V–C_{vac} curve and the vacancy aggregation morphology, we constructed a schematic diagram containing 99 atoms for interpretation (Figure 2q). Mathematically, the slope of the J_V–C_{vac} curve represents the amount of J_V change per unit vacancy concentration increase. Therefore, we examined the change of J_V after adding one S vacancy at different positions. At the initial state (case 0), the model involves 3 vacancies with discrete distribution, yielding $J_V = 91.7\%$. When a new vacancy is added to connect the originally discrete vacancies to a line (case 1), J_V significantly drops to 78.2%. It explains the first round of rapid J_V reduction (stage I) in Figure 2p, which corresponds to the morphology change of vacancies from isolated clusters to aggregated lines. On the basis of case 1, if the next vacancy attaches at the end of the vacancy line to increase its length (case 2), J_V will only decrease by 1% due to its limited influence on the coordination number change of the neighboring atoms. It indicates that the prolongation of line defects has little impact on J_V, which explains that the plateau period (stage II) in Figure 2p mainly corresponds to the elongation of S vacancy lines. If the newly added vacancy attaches to the side of the line defect to increase its width (case 3), J_V will decrease by 8%, which is significantly higher than that in case 2. It verifies that the secondary rapid decline period of J_V (stage III) in Figure 2p corresponds to the broadening behavior of the line defects.

Figure 3 tracks the dynamics of line defect elongation and broadening at the atomic scale. Figure 3a–c is consecutive AC-TEM images showing the extension of a 2SVL. The ends of the two parallel single S vacancy lines are almost flush, indicating their comparable growth velocity. We can therefore infer that the newly added vacancies are inclined to alternately attach at the terminations of two single sulfur vacancy lines. Figure 3d–f displays the process of broadening a 2SVL into a 3SVL. It is noteworthy that the widening of a line defect is realized in two steps. First, a vacancy is attached at the side of the 2SVL (Figure 3e). Second, more vacancies aggregate around the first vacancy and extend along the zigzag direction parallel to the 2SVL (green arrows in Figure 3e,f). Figure 3g is a histogram exhibiting the quantity of S vacancies contained in nSVLs (n = 2, 3, and 4) of different widths under different vacancy concentrations. The data are derived from the analysis of another large region (Figure S4, Supporting Information) that is distinct from the region discussed in Figure 2. Two results can be obtained from Figure 3g. First, with the increase in vacancy concentration, the increased number of vacancies in 2SVLs is much greater than that in other line defects with larger widths, indicating that the newly introduced vacancies mainly contribute to the extension of 2SVLs. Second, when the vacancy concentration exceeds 12%, 3SVLs and even wider line defects begin to appear, and their growth rate dramatically rises. It further verifies the vacancy concentration-dependent growth anisotropy of line defects in monolayer MoS_2, which has been discussed in Figure 2p. At low vacancy concentrations, the growth

ADVANCED
SCIENCE NEWS
www.advancedsciencenews.com
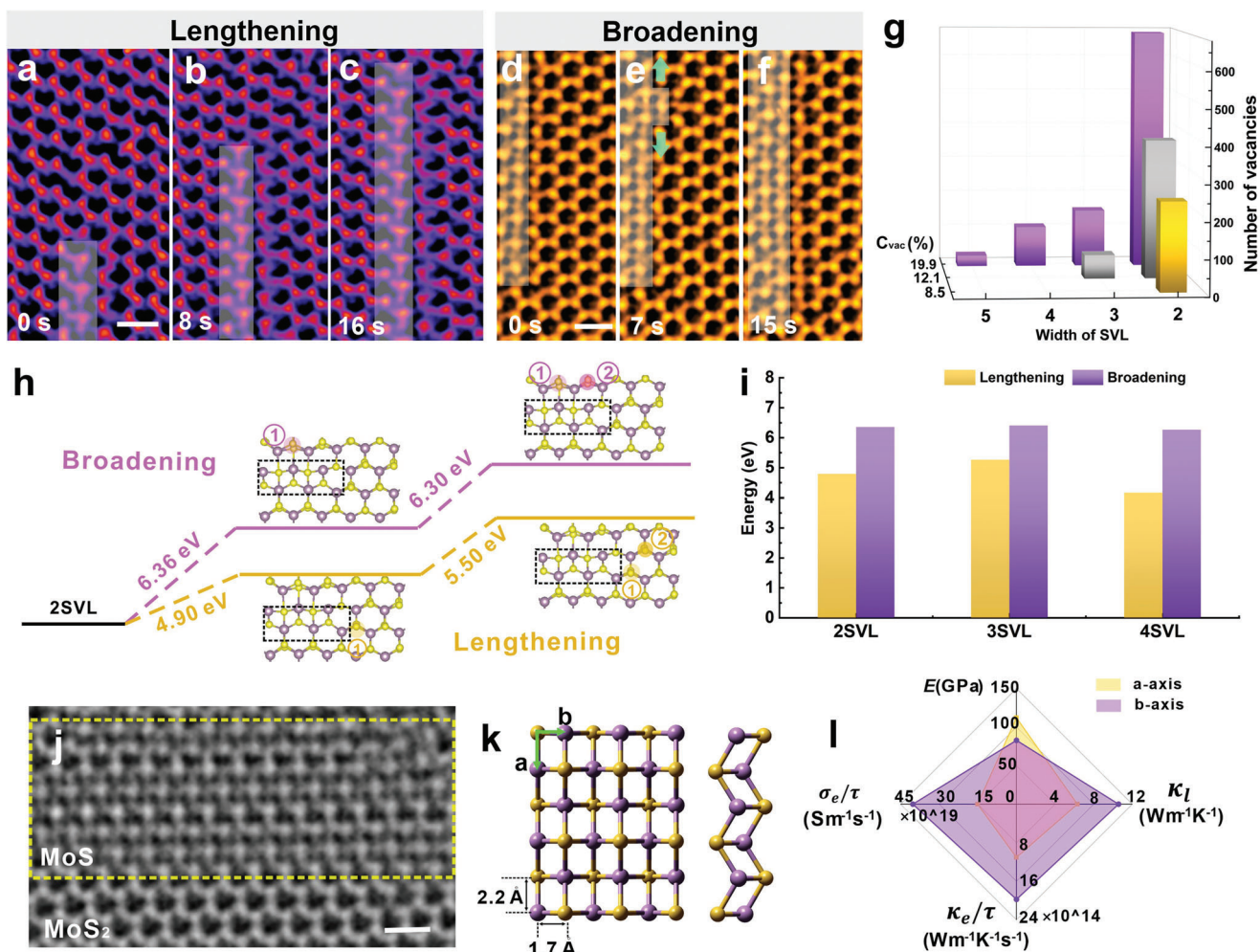
NANO · MICRO
small
www.small-journal.com

Figure 3. Growth anisotropy of S vacancy lines and the formation of low-symmetry monolayer molybdenum monosulfide (MoS) with DFT-calculated anisotropic properties. a–c) Time series of AC-TEM images showing the extension of a 2SVL. The 2SVL represents two adjacent parallel monosulfur vacancy lines along the zigzag direction. With the broadening of line defects, n adjoining monosulfur vacancy lines can be generated, which are denoted as nSVL. The location of the 2SVL is highlighted by a semi-transparent white mask. Scale bar: 0.5 nm. d–f) Time series of AC-TEM images showing the broadening of a 2SVL. Scale bar: 0.5 nm. g) Histogram displaying the total number of S vacancies contained in line defects of different widths (nSVL, n = 2, 3, and 4) under different vacancy concentrations. h) Energy profiles for lengthening and broadening of a 2SVL, respectively. i) Histogram showing the energy required to add a S vacancy at the end or side of a nSVL (n = 2, 3, and 4) for line defect lengthening and broadening, respectively. j) AC-TEM image showing the formation of monoatomic MoS layer. Scale bar: 0.5 nm. k) Projective-view and side-view of the DFT-relaxed atomic model of monolayer MoS. l) Radar map showing the anisotropy in elastic modulus (E), lattice thermal conductivity (K_l), electron thermal conductivity (K_e/τ) and electrical conductivity (σ/τ) properties of monolayer MoS along a-axis and b-axis, respectively.

of line defects is mainly manifested as the prolongation of narrow line defects such as 2SVLs. As the vacancy concentration enhances, the broadening behavior of line defects emerges and becomes common.

Density functional theory (DFT) calculations were performed to unveil the growth anisotropy of S vacancy lines along the zigzag and armchair directions. Figure 3h shows the energy required when adding two vacancies sequentially for the extension and broadening of a 2SVL, respectively. The energy required to add two vacancies sequentially on the side of a 2SVL for its broadening is 6.36 eV and 6.30 eV, respectively. In comparison, the energy needed to add two vacancies one by one at the end of a 2SVL are only 4.90 eV and 5.50 eV, respectively, which are significantly lower than those for the line defect widening (Figure S5, Sup-

porting Information). The results unravel the reason why the line defect growth along the zigzag lattice directions (i.e., elongation) is preferred over the growth along the armchair directions (i.e., broadening). Figure 3i displays the formation energy required to add one vacancy at the side or end of a nSVL (n = 2, 3, and 4, Figure S6, Supporting Information), manifesting that line defects in different widths are always thermodynamically advantageous in lengthening over broadening.

A small region of monoatomic MoS membrane was generated when the S vacancy concentration in monolayer MoS_2 is high (yellow dashed frame in Figure 3j). Distinct from the honeycomb lattice structure of hexagonal MoS_2, MoS undergoes significant compression in the a-axis direction (i.e., the armchair direction of MoS_2) and transforms into a rectangular lattice. The DFT-relaxed

**ADVANCED
SCIENCE NEWS**
www.advancedsciencenews.com

**NANO · MICRO
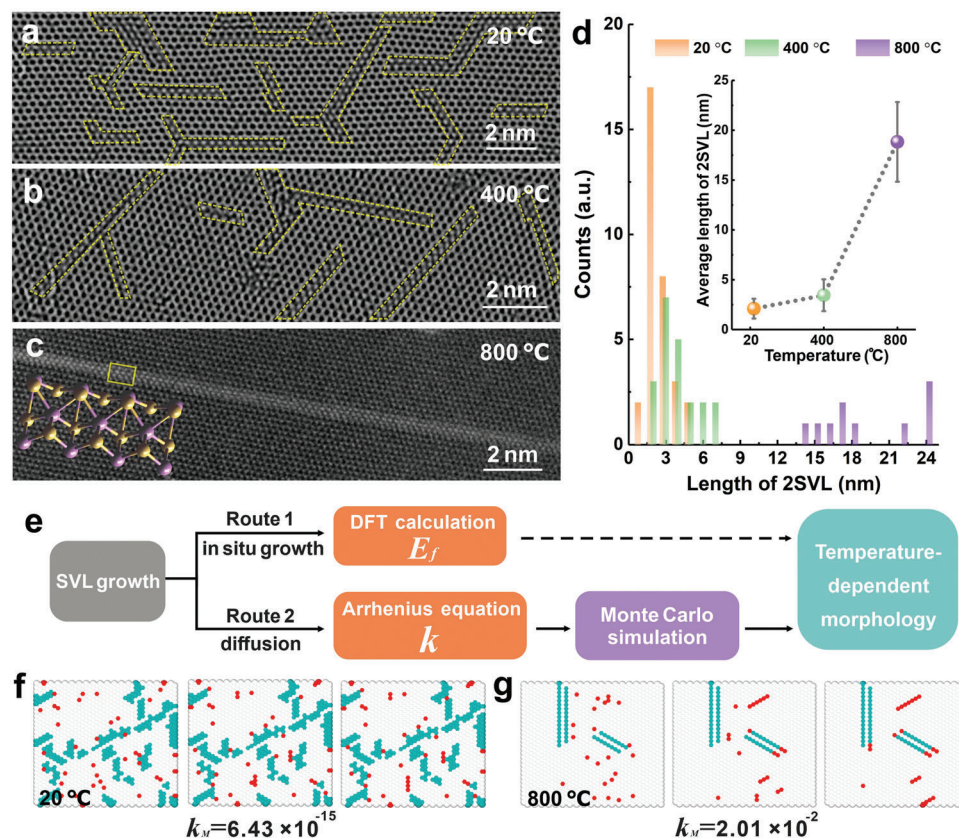small**
www.small-journal.com

Figure 4. Temperature-dependent morphology of S vacancy lines. a–c) Aberration-corrected (S)TEM images showing the morphology of S vacancy lines formed at 20 °C, 400 °C, and 800 °C, respectively. Panels a and b are AC-TEM images, while panel c is an ADF-STEM image. Vacancy lines in panels a and b are highlighted by the yellow dashed lines. The inset of panel c displays the atomic model corresponding to the line defect generated at 800 °C. d) Histogram showing the length distribution of 2SVLs formed at 20 °C, 400 °C, and 800 °C, respectively. Inset is the scatter diagram displaying the average 2SVL length grown at different temperatures. e) Logical framework for analyzing the temperature effect on the morphology of line defects. E_f represents the energy of directly generating a vacancy at the end or edge of a line defect, while k represents the vacancy diffusion rate constant estimated based on the Arrhenius equation. f,g) Monte Carlo simulation snapshots displaying the morphology of line defects formed at 20 °C and 800 °C, respectively. The green dots represent the vacancies that have already assembled into fixed line defects in the initial model, while the red dots are vacancies that are mobile during the simulation process. k_M represents the diffusion probability in the Monte Carlo simulation.

atomic models of monolayer MoS are exhibited in Figure 3k. It shows that the coordination number of Mo and S atoms in monolayer MoS is 4. The side view of the MoS model shows an undulating zigzag structure, which is disparate from monolayer MoS_2. The calculations indicate that the thermodynamically stable lattice constants a and b for monolayer MoS are 0.22 and 0.17 nm, respectively, which match well with the experimentally measured 0.21 ± 0.05 nm and 0.17 ± 0.05 nm in the AC-TEM images (Figure S7, Supporting Information). Compared with the hexagonal MoS_2, monolayer MoS belongs to the rectangular crystal system in the 2D Bravais lattice. The decreased lattice symmetry of MoS may lead to prominent property anisotropy along different crystal orientations. Figure 3l is a radar map displaying the anisotropy in elastic modulus (E), lattice thermal conductivity (K_l), electron thermal conductivity (K_e/τ), and electrical conductivity (σ/τ) of monolayer MoS along the a-axis and b-axis, respectively, based on DFT calculations. The elastic modulus of MoS in the a-axis direction is about 1.5 times higher than that along the b-axis. In contrast, the lattice thermal conductivity, electron thermal conductivity, and electrical conductivity in the b-axis di-

rection are about 2 times greater than those along a-axis. In comparison, these properties are almost the same along the armchair and zigzag directions in monolayer MoS_2 due to its high lattice symmetry (Figure S8, Supporting Information).

The growth and morphology of S vacancy lines also exhibit temperature dependence. **Figure 4**a–c shows the morphology of the line defects grown at 20 °C, 400 °C, and 800 °C, respectively, under similar vacancy concentrations. 2SVLs are dominant at all three temperatures, while the line defect configuration formed at 800 °C has a slight deviation from those generated at the other two temperatures (Figures S9 and S10, Supporting Information). The nucleation density of the S vacancy lines grown at 20 °C is high, leading to the formation of dense triangular networks. The individual line defects are short in length, uneven in width, and have many kinks under this condition (Figure 4a). When the heating temperature increases to 400 °C, the density of the line defects decreases with increased length and width uniformity for individual defects (Figure 4b). At 800 °C, the S vacancies generate smooth and ultralong line defects up to tens of nanometers in length with homogeneous configuration (Figure 4c). Figure 4d

**ADVANCED
SCIENCE NEWS**

www.advancedsciencenews.com

NANO · MICRO

small

www.small-journal.com

is a histogram displaying the length distribution of 2SVLs grown at 20 °C, 400 °C, and 800 °C, respectively, with an inset showing the average length of the line defects at these three temperatures. The average length of the line defects increases slightly from ≈2.1 to ≈3.3 nm when the growth temperature enhances from 20 to 400 °C. When the temperature reaches 800 °C, the average length of the S vacancy lines spikes to ≈20 nm. It should be noted that the initial region for TEM imaging at different heating temperatures was the well-preserved MoS$_2$ lattice, which ensures that the heating process did not affect the formation of vacancy lines.

Monte Carlo (MC) simulations combined with DFT calculations were applied to investigate the mechanism of the temperature-dependent morphology evolution of S vacancy lines. There are mainly two routes for the line defect growth (Figure 4e). First, the newly introduced vacancy is directly generated at the end or side of the line defects (Route 1). Second, the vacancy is generated in the intrinsic region and migrates to the line defect, contributing to its extension or broadening (Route 2). We first applied the DFT calculations for Route 1 (Table S1, Supporting Information). The results show that the formation energy required to generate a vacancy at the side or end of a line defect (E_f) is very similar at 20 °C and 800 °C, indicating that Route 1 is not sensitive to temperature and thus not the main cause of the temperature-dependent line defect morphology evolution. For Route 2 which is diffusion dominated, according to the Arrhenius equation,

$$k = A \cdot \exp\left(-Q/k_B T\right) \qquad (4)$$

in which k represents the diffusion rate constant of the S vacancy in monolayer MoS$_2$, A is the pre-exponential factor, Q represents the diffusion barrier of the S vacancy, k_B is the Boltzmann constant, and T is the temperature in Kelvin, the vacancy diffusion rate at 800 °C will be at least 9 orders of magnitude faster than that at 20 °C with a diffusion barrier of 0.8 eV. Therefore, the variation in vacancy diffusion at different temperatures may be the dominant reason for the temperature dependence of the line defect morphology.

We performed cluster expansion model-based MC simulations to better understand the intermediate diffusion process of S vacancies (Figure 4f,g). The green spots are fixed vacancies that have already grown into line defects in the initial model, while the red spots are vacancies that are newly added and mobile during the simulation process. Figure 4f are series of snapshots of MC simulations. It shows that S vacancies represented by the red spots move slowly at 20 °C. They either attach to the side/end of the nearby line defects or generate short new vacancy lines with only 2–3 atomic columns in length, leading to the formation of a dense and complex network structure. In contrast, the diffusion rate of the S vacancies dramatically increases together with an obvious expansion of the diffusion range when the heating temperature enhances to 800 °C (Figure 4g). The newly introduced vacancies are inclined to attach to the termination of the vacancy lines, generating a long and straight linear structure. The simulation results are consistent with the experimental observations in Figure 4a,c, further verifying that the temperature-dependent morphology change of S vacancy lines is predominantly derived from the dramatic variation in the vacancy diffusion rate at different temperatures.

The morphology of S vacancy lines is not only determined by the growth behavior but also affected by reconstruction, which was observed at both 20 °C and 800 °C (Figure S11, Supporting Information). Reconstruction results in the elimination of kinks and corners, thus promoting the smoothness and straightness of line defects. **Figure 5**a includes typical AC-TEM images showing the translation of the line defects. The left line defect (SVL-2) shifts horizontally to the right about 0.5 nm to align with the other line defect (SVL-1), eliminating the kink formed by the dislocation of the two line defect terminations. Figure 5b displays the deflection behavior of a 2SVL, where the SVL-1 is rotated clockwise 60° to align with SVL-2, thus eliminating a corner. The DFT calculations indicate that these types of reconfigurations can lead to a decrease in the system's total energy. For the S vacancy line models with the same total defect length (Figure S12, Supporting Information), translation and deflection result in the system energy reduction of 7.1 eV and 8.7 eV, respectively (Figure 5c).

We also conducted configurational force analysis to theoretically understand the force direction and the movement trend of the line defect during the reconstruction. The configurational force is defined as the partial conduction of the energy of the material configuration to the position. Here, the calculation was based on solving the full field stress distribution using Eshelby's inclusion theory (see Section S1 in the Supporting Information). According to literature reports, Eshelby's inclusion theory can be extended to the atomic scale.[52] Therefore, we constructed elliptical inclusions in a flat plate region (MoS$_2$) to represent line defects. The motion of an elliptical inclusion is mainly attributed to the configurational force component perpendicular to the major axis of the ellipse. Taking Ellipse 2 as an example, in the model corresponding to translation, the horizontal leftward configurational force component applied to Ellipse 2 makes it tend to translate to the left (Figure 5d). In the model corresponding to the deflection, the configurational force perpendicular to the major axis of Ellipse 2 will generate a torque that causes it to rotate counterclockwise (Figure 5e). It can be seen that in the final stage of translation and deflection, Ellipse 2 has no configurational force component in the horizontal direction, indicating that the state of two elliptical inclusions arranged along the same straight line is a stable state with the lowest energy. Both DFT calculations and configurational force calculations indicate that the reconstruction of linear defects to form a straight morphology is a result of energy optimization.

To figure out the intermediate process of the line defect reconstruction, we applied a high frame rate camera to continuously shoot the line defects in translation at an interval of 200 ms (Figure 5f). It is found that the translation between two adjacent line defects is not completed in one step. Instead, a piecewise translation occurs, which is manifested as a gradual downward movement of the kink from the middle to the end (the white arrows in Figure 5f). Each time the kink moves down one unit length, it intuitively shows as swapping the position between a S vacancy (α) and a disulfide atomic site (β), as shown in Figure 5g. The line defect deflection also involves complex intermediate steps (Figure S13, Supporting Information). To gain insights into the mechanism of line defect translation at the high temporal and spatial resolution, there still remain two questions to be answered: i) what is the intermediate process of switching the position of the S vacancy at the α site and the position of the

ADVANCED
SCIENCE NEWS
www.advancedsciencenews.com

NANO · MICRO
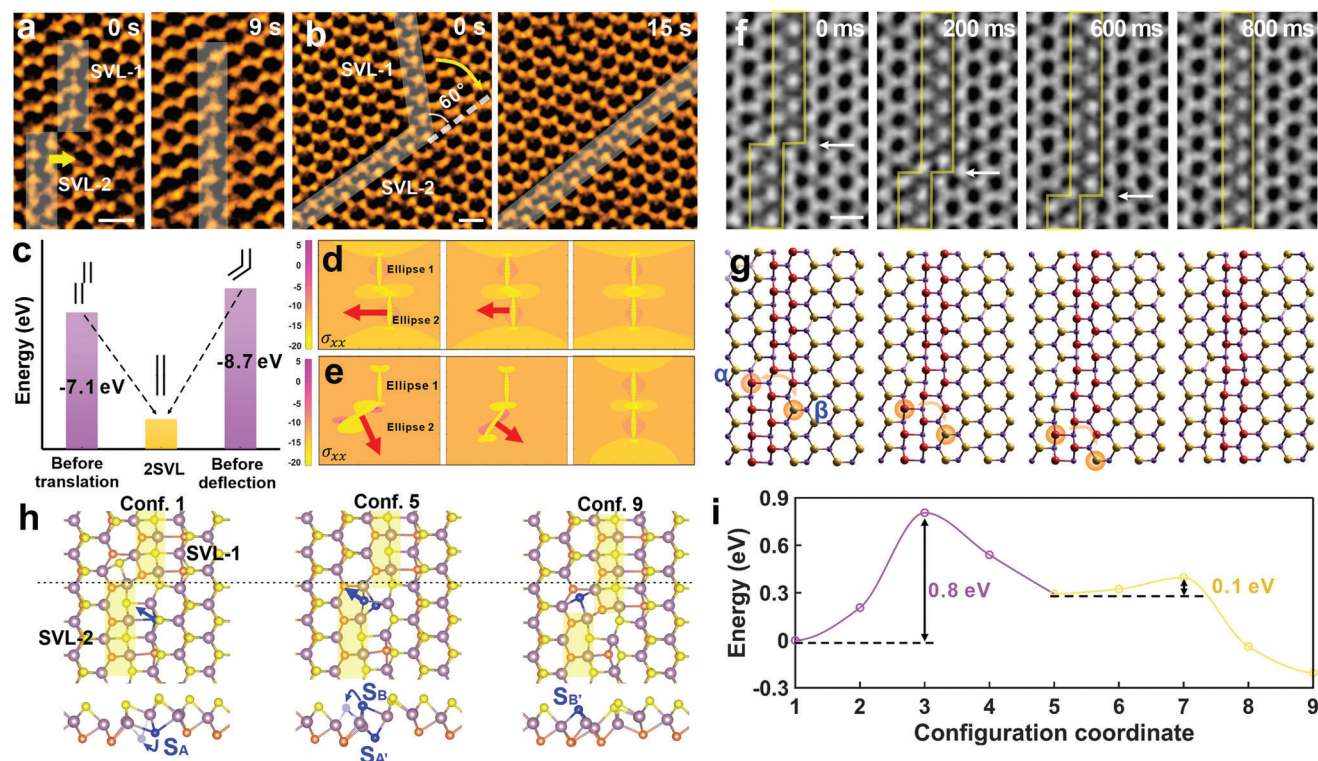**small**
www.small-journal.com

Figure 5. Reconstruction of S vacancy lines. a) Consecutive AC-TEM images showing the translation of S vacancy lines at 20 °C. Scale bar: 0.5 nm. b) Consecutive AC-TEM images showing the deflection of S vacancy lines at 20 °C. Scale bar: 0.5 nm. c) Energy reduction caused by one line defect formed after translation or deflection of two adjacent line defects. d,e) Configurational force analysis for line defect translation and deflection, respectively. Ellipses 1 and 2 represent line defects, and the remaining regions represent intrinsic MoS_2. The heat map shows the distribution of plane stress (σ_{xx}). The red arrow indicates the direction of configurational force subjected to the line defect. f) Time series of AC-TEM images captured by a high-speed camera displaying the intermediate process of line defect translation with a time interval of 200 ms at 20 °C. Scale bar: 0.5 nm. g) Atomic models corresponding to panel (f). h) DFT-calculated model showing the atomic movement during the line defect translation. i) Energy profile corresponding to the atomic movement in panel (h).

disulfide atomic column at the β site separated by a row of atoms? ii) why does the piecewise translation start with a kink of the line defect? Figure 5h displays the DFT-calculated atomic migration process during the line deflect translation with the corresponding energy profiles shown in Figure 5i. The downward movement is realized by the sequential migration of the two S atoms situated in the top and bottom atomic planes in monolayer MoS_2. The S atoms that migrate are highlighted in blue. As shown in the side view of the atomic model, the S atom (S_A) in the bottom atomic plane in Conf. 1 first slides to the left and resides at the position denoted as $S_{A'}$ in Conf. 5. The energy barrier of this process is 0.8 eV, as shown by the pink peak in Figure 5i. Subsequently, the S atom (S_B) situated in the top atomic plane in Conf. 5 moves to the left to reach the position denoted as $S_{B'}$ in Conf.9. This process only needs to overcome an energy barrier of 0.1 eV, as represented as the yellow peak in Figure 5i. Such sequential migration of the two S atoms leads to the downward shift of the line defect kink by one unit length, as can be seen from the projective view of the atomic models in Figure 5h. The energy of Conf. 9 is 0.2 eV lower than that of Conf. 1, indicating the thermodynamic advantage of this migration path. We also calculated the energy profile of another migration path, where the S atoms that migrate are far away from the kink (Figure S14, Supporting Information). Such migration path not only results in a diffusion bar-

rier of up to 2.2 eV but also leads to a higher final system energy than the initial configuration. These results unveil the reason why piecewise translation of line defects occurs at the kinks and suggest the energetically favorable atomic steps of the line defect translation.

3. Conclusion

By applying the low-voltage AC-TEM with an ultrastable in-situ heating holder and a fast frame rate camera, we unveil the vacancy concentration-dependent growth anisotropy, temperature-dependent morphology evolution, and the millisecond-scale atomistic reconstruction process of S vacancy lines in monolayer MoS_2. We transfer the concept of alloying degree to quantitatively investigate the growth mode of sulfur vacancy lines. It is discovered that the vacancy lines lengthen first and then start to widen as the vacancy densifies. This method implies that both atomic-scale structural information and large-scale statistical regularities can be obtained simultaneously through quantitative analysis of nearly a thousand atomic sites in the TEM image. At a high vacancy concentration, a small area monolayer MoS with a rectangular lattice is formed and theoretically predicted to exhibit anisotropy in mechanical, electrical, and thermal properties. When the temperature of defect generation increases from 20 to

800 °C, the defect configuration changes from dense triangular networks to ultralong and narrow lines, which is due to the significant increase in the vacancy migration rate at high temperatures. The vacancy line reconstructions, including translation and distortion, are discovered, which are realized by the sequential migration of sulfur atoms at the kink sites on the millisecond scale. These reconstructions lead to prominent energy reduction by theoretical calculations. This work provides new ideas for how to carry out the TEM study that balances the accuracy and universality of the discoveries. It also gives insights into the defect formation mechanisms and helps improve the controlled sculpture of nanomaterials, which may generate novel 2D structures with exotic properties.

4. Experimental Section

Synthesis and Transfer of Monolayer MoS₂: Monolayer MoS_2 was grown by a hydrogen-free CVD method under atmospheric pressure with molybdenum trioxide (MoO_3, ≥99.5%, Sigma-Aldrich) and sulfur (S, ≥99.5%, Sigma-Aldrich) powder used as precursors, similar to the previous reports.[53,54] SiO_2/Si (300 nm thick SiO_2) chips were used as substrates. To avoid the quench of MoO_3 powder by S vapor during the reaction, an inner tube with MoO_3 powder placed inside was inserted into the outer 1 in. quartz tube, where S powder was positioned. Two furnaces were used to give independent temperature control on both two precursors and the substrate. The typical heating temperatures for S, MoO_3 and SiO_2/Si substrate were ≈180, ≈300, and ≈800 °C, respectively. After the growth, monolayer MoS_2 was transferred to a Si_3N_4 TEM grid (Agar Scientific AG21580). A thin film of poly (methyl methacrylate) (PMMA) was first spin-coated on the $MoS_2/SiO_2/Si$ substrate surface. Subsequently, the sample was floated on a 1 mol L⁻¹ potassium hydroxide (KOH) solution to etch SiO_2 away. As soon as the PMMA/MoS_2 film detached from the Si substrate, the film was transferred to the deionized water three times to remove residuals left by the etchant thoroughly. After that, the PMMA/MoS_2 film was scooped up by a holey Si_3N_4 TEM grid, allowed to dry in the air naturally and baked at 180 °C for 15 min. The PMMA scaffold was finally removed by submerging the TEM grid in acetone for 8 h.

Transmission Electron Microscopy and Image Processing: The AC-TEM images at 20 °C were conducted by Oxford's JEOL JEM-2200MCO field emission gun TEM with a CEOS imaging aberration corrector under an accelerating voltage of 80 kV. A double Wien filter monochromator with a 7 μm slit was applied to reduce the energy spread of the electron beam to ≈ 0.21 eV. AC-TEM images were recorded by a Gatan Ultrascan 4k × 4k CCD camera with 2 s acquisition time and 2-pixel binning. The pixel resolution for each AC-TEM image is 145 pixels nm⁻¹. The high-temperature AC-TEM images at 400 °C in Figure 4b were conducted using an FEI Titan 80-300 environmental TEM under 80 kV accelerating voltage with a Gatan OneView (4k×4k) high frame rate camera. In-situ heating was achieved by a Gatan 652 Inconel heating holder, and the heating rate was 10 °C s⁻¹. The high-temperature ADF-STEM images at 800 °C in Figure 4c, Figures S10 and S11 (Supporting Information) were conducted using an aberration-corrected JEOL ARM300CF equipped with a JEOL ETA corrector.[55] The heating rate was 10 °C s⁻¹. Dwell times of 5–20 μs and a pixel size of 0.006 nm per pixel were applied for imaging with a convergence semi-angle of 31.5 mrad, a beam current of 44 pA, and inner-outer acquisition angles of 49.5–198 mrad. In situ heating was achieved using a commercially available in situ heating holder from DENS Solutions (SH30-4M-FS). Images were processed using the ImageJ software. Two types of false color LUTs, fire and orange hot, were applied to grayscale images for the enhancement of the visual effect of Pt atom dopants and dislocation cores. A Gaussian blur filter (≈2–4 pixels) was used on AC-TEM and ADF-STEM images for smoothing. Atomic models were constructed using the software of Accelrys Discovery Studio Visualizer. Multiscale image simulations for AC-TEM images were performed using the multiscale method in the JEMS software.

Density Functional Theory (DFT) Calculation: All DFT calculations were implemented in the Vienna Ab initio Simulation Package (VASP).[56,57] The exchange-correlation potential was described by Perdew-Burke Ernzerhof (PBE) functional with generalized gradient approximation (GGA).[58] The plane wave energy cutoff was 300 eV. The structural relaxations are done with the residual Hellman–Feynman force <10⁻³ eV Å⁻¹ and electronic self-consistent step convergence is 10⁻⁵ eV. The "6×12×1" Monkhorst-Pack meshes (see Figure 3k) and only one Γ point (see Figures 3h,i and 5c,h,i) were used. Based on the DFT calculation results, the lattice thermal conductivity was calculated using the Phono3py software package.[59] In addition, the BoltzTraP2 software package was used to solve the Boltzmann transport equation and obtain the electronic thermal conductivity and conductivity.[60]

Cluster Expansion Model-Based Monte Carlo Simulation: To simulate the evolution process of linear defects morphology herein, the cluster expansion model was used. For simplification, we constructed the honeycomb mesh plane only composed of non-metallic sites (Figure 4f,g). The state of a site can be described as a state variable $S_i (i = 1, 2, ..., n)$, where $S_i = 0$ means the site i was occupied by a S atom, and $S_i = 1$ means it was occupied by a vacancy. In addition, the energy of the system can be expressed as

$$E = J_0 + \sum_i J_i S_i + \sum_{j,i} J_{ij} S_i S_j + \sum_{k,j,i} J_{ijk} S_i S_j S_k + \cdots \qquad (5)$$

where J's are the interaction energies (effective cluster interactions) of various orders, and the second, third and fourth term is the summation over all sites, pairs of sites, and triples, respectively, and so on.[61] Only the nearest-neighbor interaction was considered, $J_0 = 0$, $J_i = 0$, $J_{ij} = -0.5$ eV, and $J_{ijk} = -1$, 0.5 and 0.5 eV corresponds to the angle of i-j-k to be 180°, 120°, and 60°, respectively. On this basis, the energy E of a system with a certain S vacancy distribution can be obtained by Equation (5). Then, the evolution of the whole system can be simulated using the Metropolis Monte Carlo.[62]

Considering that theoretical calculations tend to overestimate the diffusion barrier, the diffusion barrier (Q) was set as 1 eV for both 20 °C and 800 °C. To accelerate the diffusion rate in the simulation, the migration probability k_M (i.e., $k_M = \exp(\frac{-Q}{k_B T})$) was expanded by 1000 times.

Supporting Information

Supporting Information is available from the Wiley Online Library or from the author.

Conflict of Interest

The authors declare no conflict of interest.

Author Contributions

Data Availability Statement

Keywords

[1] D. Geng, H. Wang, G. Yu, *Adv. Mater.* **2015**, *27*, 2821.
[2] J. Li, M. Chen, C. Zhang, H. Dong, W. Lin, P. Zhuang, Y. Wen, B.o Tian, W. Cai, X. Zhang, *Adv. Mater.* **2019**, *31*, 1902431.
[3] Y.u Zhang, Q. Ji, J. Wen, J. Li, C. Li, J. Shi, X. Zhou, K. Shi, H. Chen, Y. Li, S. Deng, N. Xu, Z. Liu, Y. Zhang, *Adv. Funct. Mater.* **2016**, *26*, 3299.
[4] J. Li, A. Samad, U. Schwingenschlögl, B.o Tian, M. Lanza, X. Zhang, *Adv. Mater.* **2022**, *34*, 2206080.
[5] S. Wang, Y. Rong, Y.e Fan, M. Pacios, H. Bhaskaran, K. He, J. H. Warner, *Chem. Mater.* **2014**, *26*, 6371.
[6] J. Dong, L. Zhang, F. Ding, *Adv. Mater.* **2019**, *31*, 1801583.
[7] Q. Feng, N. Mao, J. Wu, H. Xu, C. Wang, J. Zhang, L. Xie, *ACS Nano* **2015**, *9*, 7450.
[8] F. Cui, C. Wang, X. Li, G. Wang, K. Liu, Z. Yang, Q. Feng, X. Liang, Z. Zhang, S. Liu, Z. Lei, Z. Liu, H. Xu, J. Zhang, *Adv. Mater.* **2016**, *28*, 5019.
[9] Z. Ma, S. Wang, Q. Deng, Z. Hou, X. Zhou, X. Li, F. Cui, H. Si, T. Zhai, H. Xu, *Small* **2020**, *16*, 2000596.
[10] P. Hu, H. Zhang, A. Li, L. Sheng, J. Jiang, Y. Yu, W. Huang, S. Li, H. Huang, J. Yu, H. Cheng, L. Mao, S. Wang, F. Ouyang, J. Zhang, *Adv. Funct. Mater.* **2023**, *33*, 2210502.
[11] W. Xu, S. Li, G. H. Ryu, P. Tang, M. Pasta, J. H. Warner, *Chem. Mater.* **2020**, *32*, 8243.
[12] Y. Wan, Z. Zhang, X. Xu, Z. Zhang, P. Li, X. Fang, K. Zhang, K. Yuan, K. Liu, G. Ran, Y. Li, Y. Ye, L. Dai, *Nano Energy* **2018**, *51*, 786.
[13] Y.u Zhang, Q. Ji, G. F. Han, J. Ju, J. Shi, D. Ma, J. Sun, Y. Zhang, M. Li, X. Y. Lang, Y. Zhang, Z. Liu, *ACS Nano* **2014**, *8*, 8617.
[14] T. Chowdhury, J. Kim, E. C. Sadler, C. Li, S. W. Lee, K. Jo, W. Xu, D. H. Gracias, N. V. Drichko, D. Jariwala, T. H. Brintlinger, T. Mueller, H. G. Park, T. J. Kempa, *Nat. Nanotechnol.* **2020**, *15*, 29.
[15] Y. Li, Z. Zhou, S. Zhang, Z. Chen, *J. Am. Chem. Soc.* **2008**, *130*, 16739.
[16] H. Zhang, Y. Yu, X. Dai, J. Yu, H. Xu, S. Wang, F. Ding, J. Zhang, *Small* **2021**, *17*, 2102739.
[17] L. Huang, F. Zheng, Q. Deng, Q. H. Thi, L. W. Wong, Y. Cai, N. Wang, C. S. Lee, S. P. Lau, T. H. Ly, J. Zhao, *Sci. Adv.* **2020**, *6*, eabc2282.
[18] S. Wang, Z. Qin, G. S. Jung, F. J. Martin-Martinez, K. Zhang, M. J. Buehler, J. H. Warner, *ACS Nano* **2016**, *10*, 9831.
[19] S. Kurasch, J. Kotakoski, O. Lehtinen, V. Skákalová, J. Smet, C. E. Krill, A. V. Krasheninnikov, U. Kaiser, *Nano Lett.* **2012**, *12*, 3168.
[20] J. Wei, B. Feng, R. Ishikawa, T. Yokoi, K. Matsunaga, N. Shibata, Y. Ikuhara, *Nat. Mater.* **2021**, *20*, 951.
[21] K. Wu, B. Chen, S. Yang, G. Wang, W. Kong, H. Cai, T. Aoki, E. Soignard, X. Marie, A. Yano, A. Suslu, B. Urbaszek, S. Tongay, *Nano Lett.* **2016**, *16*, 5888.
[22] S. Kondo, T. Mitsuma, N. Shibata, Y. Ikuhara, *Sci. Adv.* **2016**, *2*, e1501926.
[23] X. Zhao, Y. Ji, J. Chen, W. Fu, J. Dan, Y. Liu, S. J. Pennycook, W. Zhou, K. P. Loh, *Adv. Mater.* **2019**, *31*, 1900237.
[24] X. Huang, Z. Zeng, S. Bao, M. Wang, X. Qi, Z. Fan, H. Zhang, *Nat. Commun.* **2013**, *4*, 1444.
[25] A. A. Murthy, T. K. Stanev, R. Dos Reis, S. Hao, C. Wolverton, N. P. Stern, V. P. Dravid, *ACS Nano* **2020**, *14*, 1569.
[26] S. Wang, H. Li, J. Zhang, S. Guo, W. Xu, J. C. Grossman, J. H. Warner, *ACS Nano* **2017**, *11*, 6404.
[27] Q. Chen, K. He, A. W. Robertson, A. I. Kirkland, J. H. Warner, *ACS Nano* **2016**, *10*, 10418.
[28] Q. Ji, Y. Zhang, Y. Zhang, Z. Liu, *Chem. Soc. Rev.* **2015**, *44*, 2587.
[29] S. Wang, A. Robertson, J. H. Warner, *Chem. Soc. Rev.* **2018**, *47*, 6764.
[30] G. H. Ryu, R. J. Chan, *Appl. Microsc.* **2020**, *50*, 27.
[31] S. Wang, G. D. Lee, S. Lee, E. Yoon, J. H. Warner, *ACS Nano* **2016**, *10*, 5419.
[32] T. Lehnert, M. Ghorbani-Asl, J. Köster, Z. Lee, A. V. Krasheninnikov, U. Kaiser, *ACS Appl. Nano Mater.* **2019**, *2*, 3262.
[33] L. Nguyen, H. P. Komsa, E. Khestanova, R. J. Kashtiban, J. J. P. Peters, S. Lawlor, A. M. Sanchez, J. Sloan, R. V. Gorbachev, I. V. Grigorieva, A. V. Krasheninnikov, S. J. Haigh, *ACS Nano* **2017**, *11*, 2894.
[34] H. P. Komsa, A. V. Krasheninnikov, *Adv. Electron. Mater.* **2017**, *3*, 1600468.
[35] L. Wang, X. Liu, Q. Zhang, G. Zhou, Y. Pei, S. Chen, J. Wang, A. M. Rao, H. Yang, B. Lu, *Nano Energy* **2019**, *61*, 194.
[36] M. Tang, W. Yin, S. Liu, H. Yu, Y. He, Y. Cai, L. Wang, *Crystals* **2022**, *12*, 1218.
[37] X. Li, S. Zhang, H. Huang, L. Hu, F. Liu, Q. Wang, *Nano Lett.* **2019**, *19*, 6005.
[38] H. P. Komsa, S. Kurasch, O. Lehtinen, U. Kaiser, A. V. Krasheninnikov, *Phys. Rev. B* **2013**, *88*, 035301.
[39] S. Fang, Y.i Wen, C. S. Allen, C. Ophus, G. G. D. Han, A. I. Kirkland, E. Kaxiras, J. H. Warner, *Nat. Commun.* **2019**, *10*, 1127.
[40] T. K. Patra, F. Zhang, D. S. Schulman, H. Chan, M. J. Cherukara, M. Terrones, S. Das, B. Narayanan, S. K. R. S. Sankaranarayanan, *ACS Nano* **2018**, *12*, 8006.
[41] S. De Graaf, B. J. Kooi, *2D Mater.* **2022**, *9*, 015009.
[42] Q. Chen, H. Li, S. Zhou, W. Xu, J. Chen, H. Sawada, C. S. Allen, A. I. Kirkland, J. C. Grossman, J. H. Warner, *ACS Nano* **2018**, *12*, 7721.
[43] X. Wang, X. Guan, X. Ren, T. Liu, W. Huang, J. Cao, C. Jin, *Nanoscale* **2020**, *12*, 8285.
[44] J. Köster, M. Ghorbani-Asl, H. P. Komsa, T. Lehnert, S. Kretschmer, A. V. Krasheninnikov, U. Kaiser, *J. Phys. Chem. C* **2021**, *125*, 13601.
[45] K. Elibol, T. Susi, G. Argentero, M. Reza Ahmadpour Monazam, T. J. Pennycook, J. C. Meyer, J. Kotakoski, *Chem. Mater.* **2018**, *30*, 1230.
[46] H. P. Komsa, J. Kotakoski, S. Kurasch, O. Lehtinen, U. Kaiser, A. V. Krasheninnikov, *Phys. Rev. Lett.* **2012**, *109*, 035503.
[47] X. Liu, T. Xu, X. Wu, Z. Zhang, J. Yu, H. Qiu, J. H. Hong, C. H. Jin, J. X. Li, X. R. Wang, L. T. Sun, W. Guo, *Nat. Commun.* **2013**, *4*, 1776.
[48] B. J. Hwang, L. S. Sarma, J. M. Chen, C. H. Chen, S. C. Shih, G. R. Wang, D. G. Liu, J. F. Lee, M. T. Tang, *J. Am. Chem. Soc.* **2005**, *127*, 11140.
[49] Y. Gong, Z. Liu, A. R. Lupini, G. Shi, J. Lin, S. Najmaei, Z. Lin, A. L. Elías, A. Berkdemir, G.e You, H. Terrones, M. Terrones, R. Vajtai, S. T. Pantelides, S. J. Pennycook, J. Lou, W.u Zhou, P. M. Ajayan, *Nano Lett.* **2014**, *14*, 442.
[50] D. O. Dumcenco, H. Kobayashi, Z. Liu, Y. S. Huang, K. Suenaga, *Nat. Commun.* **2013**, *4*, 1351.

[51] T. Xu, S. Li, A. Li, Y. Yu, H. Zhang, P. Hu, W. Zhou, L. Sheng, T. Jiang, H. Cheng, X. Cheng, F. Ouyang, J. Zhang, S. Wang, *Small Struct.* **2022**, *3*, 2200025.

[52] F. Liu, T. C. Wang, Q. Tang, *Small* **2018**, *14*, 1703512.

[53] S. Li, S. Wang, T. Xu, H. Zhang, Y. Tang, S. Liu, T. Jiang, S. Zhou, H. Cheng, *Nanoscale* **2021**, *13*, 13030.

[54] S. Wang, X. Wang, J. H. Warner, *ACS Nano* **2015**, *9*, 5246.

[55] F. Hosokawa, H. Sawada, Y. Kondo, K. Takayanagi, K. Suenaga, *Microscopy* **2013**, *62*, 23.

[56] G. Kresse, J. Furthmüller, *Phys. Rev. B* **1996**, *54*, 11169.

[57] G. Kresse, J. Furthmüller, *Comput. Mater. Sci.* **1996**, *6*, 15.

[58] J. P. Perdew, K. Burke, M. Ernzerhof, *Phys. Rev. Lett.* **1996**, *77*, 3865.

[59] A. Togo, L. Chaput, I. Tanaka, *Phys. Rev. B* **2015**, *91*, 094306.

[60] G. K. H. Madsen, J. Carrete, M. J. Verstraete, *Comput. Phys. Commun.* **2018**, *231*, 140.

[61] J. M. Sanchez, F. Ducastelle, D. Gratias, *Phys. A* **1984**, *128*, 334.

[62] N. Metropolis, A. W. Rosenbluth, M. N. Rosenbluth, A. H. Teller, E. Teller, *J. Chem. Phys.* **1953**, *21*, 1087.